https://doi.org/10.5194/egusphere-2026-51
Preprint. Discussion started: 20 January 2026

Evaluation of UAV-based methods for quantifying methane point source emissions

Abdullah Bolek[1], Meghan N. Beattie[2], Jalal Norooz Oliaee[2], Roger MacLeod[3], June Skeeter[3], Peter Morse[3], Martin Heimann[1], and Mathias Göckede[1]

[1]Max Planck Institute for Biogeochemistry, Department of Biogeochemical Signals, Jena, Germany
[2]Metrology Research Centre, National Research Council Canada, Ottawa, Canada
[3]Geological Survey of Canada, Natural Resources Canada, Ottawa and Sidney, Canada

Correspondence: Abdullah Bolek (abolek@bgc-jena.mpg.de)

Abstract. Uncrewed aerial vehicles (UAVs) are increasingly becoming essential monitoring tools across a rapidly growing set of applications, due to their operational versatility, relatively low operating cost, and provision of data at a range of spatial scales. However, UAV-based measurement methodologies and associated instruments for atmospheric research are still in their early stages and require extensive efforts to exploit their full potential. In Arctic regions, geological CH_4 seeps can release CH_4 at rates significantly higher than typical biogenic sources and those associated with permafrost degradation processes; hence, accurate quantification of their emission rates is crucial for the overall CH_4 budget of the Arctic. The application of conventional greenhouse gas monitoring platforms—flux chambers and eddy-covariance towers—may become impractical as eddy-covariance towers are stationary point measuring devices that require long observation times with reliable footprint modeling to constrain emissions while flux chambers have a small footprints and therefore require multiple measurements and have a high potential of introducing disturbances. UAVs can overcome these limitations as they can capture the spatial extent of the gas plume released from a point source with minimal disturbance to the source. In July 2025, we deployed two UAV platforms with different sensing instruments to sample a known geological CH_4 seep located at the Mackenzie River Delta, Canada. We flew vertical "curtain" patterns with open-path and closed-path CH_4 instruments to sample gas concentrations in flux planes at different downwind distances from the gas seep. We first evaluated the performance of the UAV-mounted instrumentation, comparing the open- and closed-path greenhouse gas analyzers. We then compared two widely used quantification techniques—mass-balance and Gaussian plume inversion—finding that mass-balance approaches yielded the most robust quantification with smaller uncertainties. We estimate that the seep emission rate falls in the range of 7.1 to 16.2 $\mathrm{kgCH_4\ h^{-1}}$, with an average estimated rate of $11.4 \pm 6.8\ \mathrm{kgCH_4\ h^{-1}}$. The emissions from this single point are equivalent to the biogenic flux from approximately 2.2 $\mathrm{km^2}$ of the surrounding permafrost landscape, underscoring the need to assess the potentially significant contribution of geological seeps to regional and pan-Arctic carbon budgets.

https://doi.org/10.5194/egusphere-2026-51
Preprint. Discussion started: 20 January 2026

1 Introduction

Arctic permafrost ecosystems are subjected to warming about four times faster than the global average (i.e., Arctic amplification) (Rantanen et al., 2022), which results in accelerated permafrost degradation that may cause the decomposition of previously frozen carbon, amplifying the release of greenhouse gases (GHGs) such as CO_2 and CH_4. Additionally, permafrost and glaciers act as natural barriers that play a critical role in trapping large amounts of geological CH_4 below ground (Walter Anthony et al., 2012). As permafrost becomes unstable due to warming, this natural barrier is compromised. Fractures and conduits can develop or expand, facilitating the release of geological CH_4 into the atmosphere (Walter Anthony et al., 2012).

Geological CH_4 seeps are abundant in the outer Mackenzie River Delta, frequently observed within channels, rivers, marshes, and lakes (Wesley et al., 2023; Walter Anthony et al., 2012; Dallimore et al., 2024). This collocation of seeps with bodies of water constrains the methods that one can apply to quantify emissions, primarily due to limited accessibility and the risk of disturbing the source during the measurements. Thus far, locating and estimating the emission flux from these under water seeps has been challenging. Aerial imaging spectroscopy is poorly suited for this application due to water's extremely low reflectance in the shortwave infrared (Zhang et al., 2017; Baskaran et al., 2022; Ayasse et al., 2018; Elder et al., 2019). Airborne eddy covariance analysis lacks the spatial resolution that is required to resolve these point sources (Kohnert et al., 2017). Furthermore, conventional surface-based monitoring systems such as eddy covariance towers or flux chambers are impractical for locating and identifying new point or localized sources, and are generally more difficult to establish on bodies of water, wetlands, and marshlands. Accurately estimating the emission rates from point or localized sources is only possible if the locations are already known, allowing monitoring systems to be positioned such that sources fall within their spatial coverage.

In contrast, small uncrewed aerial vehicles (UAVs) equipped with in-situ gas instruments are a very practical measurement alternative that can access hard-to-reach areas over bodies of water, wetlands, and marshlands. Small UAVs create minimal disturbance and can map the entire extent of a plume originating from a point source. Despite current limitations in their flight time, small UAVs are becoming an essential tool in atmospheric science (Thielicke et al., 2021; Wildmann and Wetz, 2022; Wetz et al., 2023, 2021; Bolek and Testik, 2022) and GHG emission measurements (Andersen et al., 2018, 2023; Gålfalk et al., 2021; Bolek et al., 2024; Bonne et al., 2023; Kunz et al., 2018, 2020; Shah et al., 2020; Scheller et al., 2022; Morales et al., 2022). Significant progress has been achieved in UAV-based emission quantification over industrial sites such as power plants and landfills (Shah et al., 2019; Gålfalk et al., 2021; Morales et al., 2022), however methodologies over natural ecosystems are still in the early stages of development (Bolek et al., 2024; Scheller et al., 2022; Shaw et al., 2021; Yazbeck et al., 2025).

Instrumentation for UAV-based GHG measurements must have high sensitivity, low power consumption, fast response time, and be lightweight. Gas analyzers based on absorption spectroscopy in the mid-infrared region using tunable diode lasers can meet these requirements and this is becoming a widely used technique to quantify the concentration of GHGs. For fast-moving aerial vehicles, such as UAVs, a critical choice must be made between open- and closed-path gas analyzers. While both rely on the same fundamental measurement principle, their gas sampling approaches differ, which influences data characteristics and processing requirements. The measuring cell of the open-path analyzers is directly exposed to the atmosphere, allowing

https://doi.org/10.5194/egusphere-2026-51
Preprint. Discussion started: 20 January 2026

near-instantaneous response to rapid changes in concentration caused by turbulence. Conversely, the enclosed sample cell in closed-path analyzers effectively smooths the measured concentration profiles due to the much lower air exchange rate in the sample cell and sampling tubes (Detto et al., 2011; Takriti et al., 2021). Closed-path analyzers typically feature temperature- and pressure-controlled sample cells, which minimize the impact of variable environmental conditions on measurement accuracy. However, the necessary sampling pumps and thermal regulation systems increase instrument weight and power consumption compared to open-path alternatives. Conversely, open-path analyzers are directly exposed to changing atmospheric conditions that can affect their performance, often requiring post-acquisition corrections.

Beyond monitoring system considerations, the choice of data analysis method is critical for accurately quantifying fluxes. One well-established technique to quantify emission rates from mobile platforms is the mass balance approach (Morales et al., 2022; Andersen et al., 2023; Bonne et al., 2023). In this method, the emission rate is estimated by integrating the enhanced concentration signal over the observational plane (Bonne et al., 2023). This method usually requires interpolation of the non-uniform sparse UAV measurements onto a uniform 2D-grid using techniques such as the Kriging method (Morales et al., 2022; Andersen et al., 2021). Fitting a covariance model to a geo-spatial dataset requires the user to optimize predefined variances and length scales, as the covariance model is highly sensitive to these parameters (Morales et al., 2022). The mass balance technique can also be applied without using a complicated interpolation scheme, provided that the collected data have high spatial resolution (Bonne et al., 2024; Scheutz et al., 2025; Borchardt et al., 2025). In this direct approach, horizontal flight transects are treated individually, and transect-integrated flux densities are interpolated between each transect, and extrapolated between the lowest-altitude transect and the ground. Gaussian plume inversion is another widely used approach to quantify the emission rates using UAVs (Shah et al., 2019; Andersen et al., 2021). In this technique, the concentration profile generated by emissions from a constant point source is assumed to be time-invariant and to follow a Gaussian distribution. UAV-based sampling close to the source may not always yield a Gaussian-like concentration field due to small-scale turbulence, short observation times, and insufficient repeated measurements; however, several studies have shown that this method can be used to generate reasonable flux estimates (Shah et al., 2019, 2020; Andersen et al., 2021). Both the Gaussian plume inversion and mass balance approaches require wind speed data in addition to concentration measurements.

In this study, we deployed two UAV platforms, one equipped with an open-path instrument and the other with a closed-path instrument, to quantify the source strength of a geological CH_4 seep. We applied three emission rate quantification methods to the measured data: mass balance with Kriging interpolation, direct mass balance, and Gaussian plume inversion. Finally, we compared the results obtained from the two gas analyzers and the different quantification methods, evaluating their advantages and disadvantages for UAV-based applications.

2 Methods

2.1 Measurement site, UAV platforms, and sampling strategies

Our study site is a known CH_4 seep of geologic origin located within the outer Mackenzie River Delta, west of Richards Island, Northwest Territories, Canada (69.319583° N, -135.477520° W), Fig. 1 (a). The permafrost underlying the delta is relatively

https://doi.org/10.5194/egusphere-2026-51
Preprint. Discussion started: 20 January 2026

thin (< 100 m) as it was formed during the Holocene and there is an abundance of water bodies (Burn and Kokelj, 2009; Dallimore et al., 2024). While several parameters influence the permafrost thermal state, including snow cover, vegetation, and ground temperature, hydrology exerts the greatest influence on the local ground thermal regime (Burn et al., 2009; Burn and Kokelj, 2009; Miner et al., 2022). We focus on a seep that was previously identified and named as Channel Seep 2 (Wesley et al., 2023; Dallimore et al., 2024), which originates from the river bed with a very high ebullition rate (see Fig. 1 (b)). Across the outer Mackenzie River Delta, Dallimore et al. (2024) documented 46 natural gas seeps with diverse characteristics in geological formation via isotopic signatures, occurrence, and size. Strong CH_4 emissions throughout this thin permafrost area were previously detected by the Polar 5 research aircraft (Kohnert et al., 2017) and attributed to geological sources based on emission rates much higher than typical biogenic sources. This attribution was later confirmed by isotopic analysis (Dallimore et al., 2024; Wesley et al., 2023).

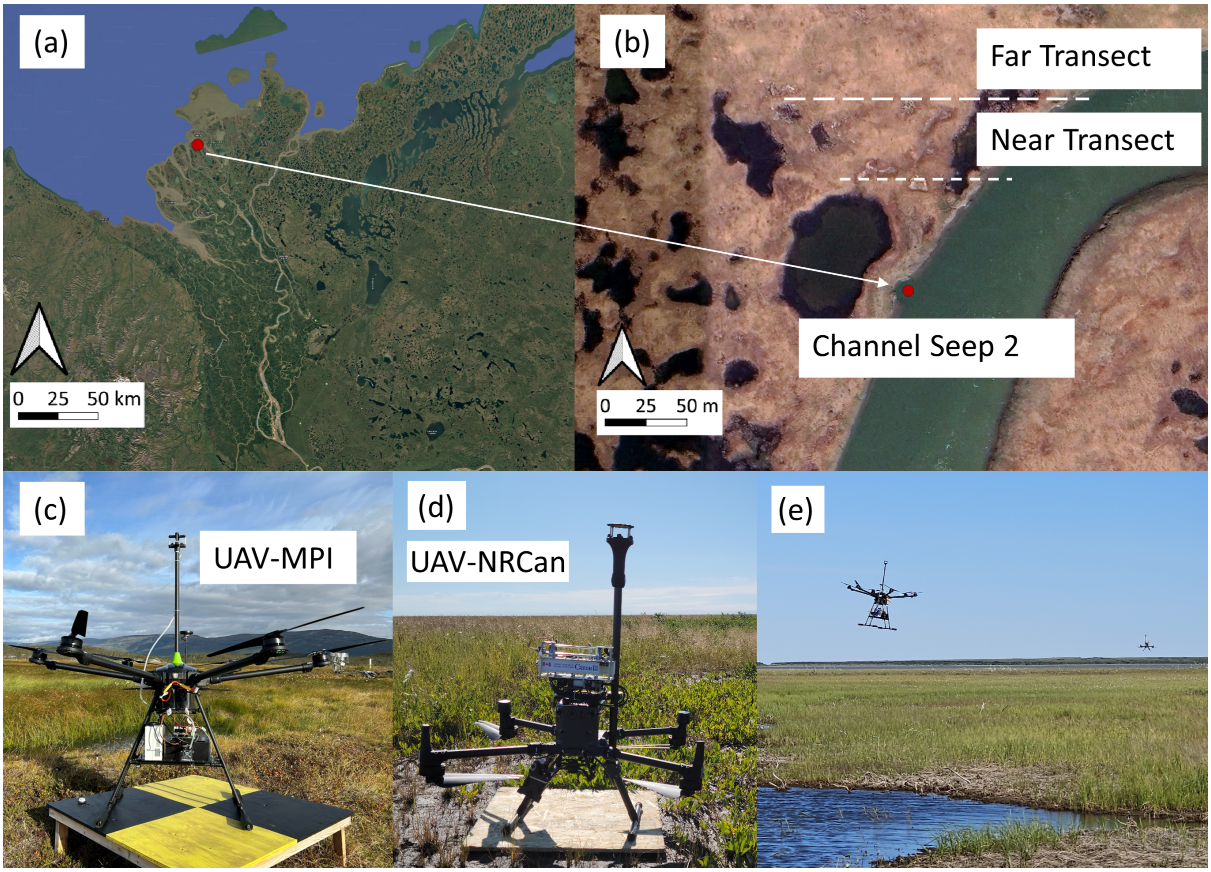

Figure 1. Study area in the outer Mackenzie River Delta, NT, Canada (a); Aerial image of the location of Channel Seep 2 (69.319583° N, 135.477520° W) indicated by red dot and approximate transects flown indicated by dashed lines (b) ((a) and (b) overlaid on satellite images from ©Google Maps); Images showing the two UAV platforms, UAV-MPI (c) and UAV-NRCan (d). Image (e) shows the two UAVs sampling downwind of CH_4 seep in the near (UAV-MPI) and far (UAV-NRCan) distances.

https://doi.org/10.5194/egusphere-2026-51
Preprint. Discussion started: 20 January 2026

To quantify the emission rate at Channel Seep 2, we used two UAV platforms: UAV-MPI (Fig. 1 (c)) and UAV-NRCan (Fig. 1 (d)). UAV-MPI is a hexacopter (PM X6 Pro XL) that is equipped with CH_4 and CO_2 gas analyzers along with an ultrasonic anemometer (Licor LI-550) that measures 2D wind speed, temperature, humidity, and pressure (see Bolek et al. (2024) for more details). The CH_4 analyzer is a closed path (CP) analyzer (Strato, Aeris Technologies) that measures the dry mole fraction of CH_4 at 2 Hz sampling frequency with $< 1\ \mathrm{ppb\,s^{-1}}$ of sensitivity. The CP instrument was customized by adding a thermally controlled enclosure to control the temperature of the measuring cell, which reduces the instrument drift (see Appendix A). The anemometer deployed on UAV-MPI recorded wind measurements at 2 Hz with a reported accuracy of $\pm 0.2\ \mathrm{m\,s^{-1}}$ for speed and ± 1.0 °for direction. UAV-NRCan is a DJI Matrice 300 RTK quadcopter equipped with a custom-built CH_4 gas analyzer and a 2D anemometer (WindUltra, Gill Instruments) to measure wind speed and direction. The CH_4 analyzer is a mid-infrared tunable diode laser absorption spectroscopic system with an open path (OP) gas cell, a sampling rate of 100 Hz, and a resolution of 26 ppb at 10 Hz, calibrated over the concentration rage of 2 ppm to 50 ppm. The Gill WindUltra anemometer on UAV-NRCan has an accuracy of $< 2\%$ RMSE for wind speed and < 1.0 °RMSE for wind direction. Two additional ground-based wind sensors were deployed to verify the UAV-based measurements. UAV-based wind speed and direction measurements showed good agreement with the ground-based measurements (data not shown). With the full scientific payload, each UAV platform achieved flight times of about 20 minutes.

We conducted a total of four flights, with each UAV platform flying curtains at two distances from the Channel Seep 2, corresponding to roughly 80 m and 150 m downwind (Fig. 1 (b)). Table 1 shows the flight details. Flight curtains were oriented to be approximately perpendicular to the local wind direction. The lowest flight transects were conducted as close to the ground surface as possible to minimize quantification uncertainty associated with a near-ground measurement gap. UAV-MPI (flight IDs CP-1 and -2) was flown manually, since programming flight pattern on-site was not convenient for this UAV, at a constant speed while maintaining a fixed heading. UAV-NRCan (flight IDs OP-1 and -2) was flown with a pre-programmed flight trajectory where the heading aligned with the direction of UAV travel. The width of the far curtains for both platforms (CP-1 and OP-1) was approximately 250 m. The near curtain width (CP-2 and OP-2) was approximately 150 m.

Table 1. Details of the conducted flights, all flights were performed on August 1, 2025. Mean air temperature during flights was about 19 °C.

Flight ID	Start Time (UTC)	End Time (UTC)	UAV Platform	Sensor Type	Downwind Distance (m)	Altitude (m)	Wind Incidence	Cruising Speed (m s^{-1})
CP-1	15:17:45	15:35:27	UAV-MPI	Closed-path	163	2 - 25	17.3°	2-3
CP-2	15:49:34	16:08:20	UAV-MPI	Closed-path	87	2 - 14	17.3°	2-3
OP-1	15:48:18	16:05:28	UAV-NRCan	Open-path	149	2.5 - 25	7.5°	7
OP-2	15:26:19	15:36:57	UAV-NRCan	Open-path	77	2.5 - 17.5	7.5°	5

https://doi.org/10.5194/egusphere-2026-51
Preprint. Discussion started: 20 January 2026

All four curtain flight transects are shown in a top-down "bird's-eye" view in Fig. 2. The x-axis is defined to align with the mean prevailing wind direction for all flights, which is $188.5°$. The downwind distance from the source (i.e., seep location) to each flux curtain along the x-axis is indicated. Along the central axis, the curtains flown by closed-path UAV-MPI (CP-1 and CP-2) are 10-14 m farther from the source than the corresponding curtains for open-path UAV-NRCan (OP-1 and OP-2), but in all cases the flight transects extended beyond the boundaries of the plume. In all curtains, the dominant wind direction approximately coincides with the location of the observed CH_4 peak enhancements along the transects. The mean wind incidence angle was < 20°in all cases (see Fig. 2 and Table 1) and the non-zero wind incidence angle is expected to have a negligible impact on the emission rate calculation (Mohammadloo et al., 2025).

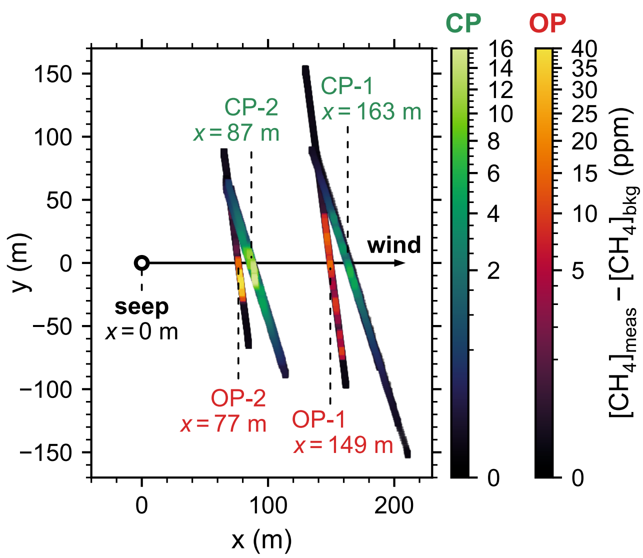

Figure 2. Bird's-eye view of measured methane concentrations after removing the background for the four curtain flights. The origin of the coordinate system is defined at the gas seep (69.319583°, -135.477520°) and the x-axis is aligned with the dominant wind direction (188.5°). Here, OP and CP indicate open-path and closed-path and refer to UAV-NRCan and UAV-MPI, respectively.

2.2 Flux quantification methods

2.2.1 Mass balance approach

The mass balance approach is widely used to estimate net emissions released from a point source or a defined area, and the mass conservation equation is typically simplified by neglecting diffusion and assuming the plume is statistically stationary during the sampling period. We applied a mass balance approach to UAV-based sampling similar to the approach used in piloted aircraft-based sampling (Karion et al., 2013; Fiehn et al., 2020). The mass balance method applied to piloted aircraft-based sampling often requires —or assumes— vertically well-mixed boundary layer since measuring plumes vertical variability is not always possible (Karion et al., 2013; Fiehn et al., 2020). Although at sufficiently downwind distances this assumption

https://doi.org/10.5194/egusphere-2026-51
Preprint. Discussion started: 20 January 2026

may hold, for UAVs where the sampling being made close to the source, the plume is most likely not vertically well-mixed, hence dense sampling along vertical and horizontal axes are required (Shaw et al., 2021). The net emission flux (Q) through a sampling plane transecting the plume is given by:

$$Q = \int\int q_{\mathrm{meas}}(y', z)dy'dz \tag{1}$$

where the flux plane is defined along the measured transect (y') and altitude (z), and $q_{\mathrm{meas}}(y', z)$ is the $\mathrm{CH_4}$ flux density at each point in the flux plane, as defined in Eq. 2 below. Note that y' is curtain-specific, as it is derived from the UAV's flight path. The flux densities are given by

$$q_{\mathrm{meas}}(y', z) = \left([\mathrm{CH_4}]_{\mathrm{meas}}(y', z) - [\mathrm{CH_4}]_{\mathrm{bkg}}\right) \cdot u_{\perp}(y', z) \cdot \rho_{\mathrm{CH_4}}(z) \tag{2}$$

where $[\mathrm{CH_4}]_{\mathrm{meas}}$ is the measured $\mathrm{CH_4}$ mixing ratio, $[\mathrm{CH_4}]_{\mathrm{bkg}}$ is the background mixing ratio, $u_{\perp}$ is the component of the recorded wind speed perpendicular to the flux curtain, and $\rho_{\mathrm{CH_4}}(z)$ is the density of $\mathrm{CH_4}$ gas, used to convert the $\mathrm{CH_4}$ mixing ratio [ppm] to mass concentration [$\mathrm{gCH_4m^{-3}}$], whichis calculated according to

$$\rho_{\mathrm{CH_4}}(z) = \frac{P(z)M_{\mathrm{CH_4}}}{R\,T_{\mathrm{avg}}} \tag{3}$$

where $P(z)$ is the altitude-dependent pressure, $M_{\mathrm{CH_4}}$ is the molar mass of $\mathrm{CH_4}$ ($16.04\,\mathrm{gmol^{-1}}$), R is the universal gas constant ($8.314\ \mathrm{m^3PaK^{-1}mol^{-1}}$), and T_{avg} is the average temperature. $P(z)$ and T_{avg} are measured during the experiment on board the UAV.

In this study, we used two different mass balance approaches to estimate the emission rate: direct mass balance (DMB), Section 3.2.1, and cluster Kriging mass balance (CKMB), Section 3.2.2. The DMB approach uses the measured enhancements without any in-plane interpolations. In DMB, transect integrated flux densities ($\int q_{\mathrm{meas}}dy'$ in $\mathrm{gCH_4s^{-1}m^{-1}}$) are calculated using simple linear interpolation, for each horizontal transect and then subsequent integration carried out in the vertical direction. At the lowest level of the sampling plane, we used a logarithmic function to complete the vertical profile, assuming zero flux at the ground level (Bonne et al., 2024). The CKMB approach, on the other hand, uses Kriging interpolation to map the measured $\mathrm{CH_4}$ enhancement onto a regular grid. Kriging is a technique that employs an interpolation based on predefined covariance models (Müller et al., 2022). We used the cluster Kriging method that was developed by Morales et al. (2022) and first clustered the data into two groups—enhanced and background—using a Gaussian Mixture Model. We fit the data within each cluster with a variogram (scikit-gstat analysis module was used), optimizing the variance and length-scales through least-square regression. We exported the fitted variograms to covariance models (gstools library), which we later used to apply Ordinary Kriging (pykrige library). We interpolated the measured wind field onto the same grid as the concentrations; however in this case, we applied ordinary Kriging without clustering the data as clustering is not required for wind data.

In both mass balance approaches, uncertainties are attributed to instrument errors, interpolation errors, plume capture uncertainty, and non-stationary plume dynamics. We quantified the instrument errors using error propagation based on field

https://doi.org/10.5194/egusphere-2026-51
Preprint. Discussion started: 20 January 2026

measurement data as well as laboratory tests. In the CKMB method, the uncertainties are quantified using the covariance matrices provided by the Kriging algorithms, which were below 10% of the calculated emission rates for all cases. For the DMB method, the uncertainties associated with linear interpolation along the vertical axis are estimated to be around 10% based on the Kriging algorithm uncertainties. Plume capture uncertainty arises when the UAV misses the plume on one or more transects. Here, we quantify this uncertainty by leaving one transect out and running the algorithm again. The estimated flux values are about 20% smaller when the transect with the highest CH_4 enhancement is excluded. Overall, we conservatively estimate the uncertainty contribution from the plume capture component to be 25% of the calculated flux values. The uncertainties originating from the turbulent nature of the atmospheric transport however, are challenging to quantify and were not included in the uncertainty estimation here.

2.2.2 Gaussian plume inversion approach

The Gaussian plume model provides a simplified solution for the advection-diffusion equation and is used to simulate the atmospheric transport of GHGs such as CH_4. In the Gaussian plume model, the concentration field is assumed to be steady-state, meaning that the wind field is stable over time such that the concentration field is time invariant. However, this assumption may not hold under turbulent and variable wind conditions, especially close to the source (Shah et al., 2019). Several formulations have been proposed to overcome this issue, such as replacing the diffusivity parameter with a near-field mixing factor (Shah et al., 2019) or incorporating variable wind direction into the model (Vergassola et al., 2007; van Hove et al., 2025). Here, we adapt the approach from Shah et al. (2019) where the time-averaged flux density is presumed to follow from the morphology of a Gaussian plume, such that the modeled flux density (q_{mod}) is given by

$$q_{\mathrm{mod}}(x,y,z) = \frac{Q}{2\pi\sigma_y(x)\sigma_z(x)} \exp\left(-\frac{(y-y_0)^2}{2\sigma_y^2(x)}\right) \left\{ \exp\left(-\frac{(z-h)^2}{2\sigma_z^2(x)}\right) + \exp\left(-\frac{(z+h)^2}{2\sigma_z^2(x)}\right) \right\} \tag{4}$$

where Q is the total emission flux from the CH_4 source, $\sigma_y(x)$ and $\sigma_z(x)$ are the horizontal and vertical mixing factors, y_0 is the center of the plume along the y-axis, and h is the height of the emission source. We assume that the mixing factors $\sigma_y(x)$ and $\sigma_z(x)$ vary linearly with distance x from the source, such that $\sigma_y(x) = \tau_y x$ and $\sigma_z(x) = \tau_z x$.

Given experimentally determined flux densities over a measured flux curtain, the emission rate through the flux curtain can be estimated by fitting Eq. 4 to the measured data. The flux densities can be computed from measured concentration data $[\mathrm{CH_4}]_{\mathrm{meas}}$ according to:

$$q_{\mathrm{meas}}(x,y,z) = \left([\mathrm{CH_4}]_{\mathrm{meas}}(x,y,z) - [\mathrm{CH_4}]_{\mathrm{bkg}}\right) \cdot u_x(x,y,z) \cdot \rho_{\mathrm{CH_4}}(z) \tag{5}$$

This definition is similar to that for flux density given in Eq. 2, except that we replace the perpendicular wind speed with u_x, which is the x-component of instantaneous wind vector, where x is aligned with the prevailing wind direction (see Fig. 2). In this work, the CH_4 source is a gas seep in a water channel, and so we fix $h = 0$. We fit the remaining parameters Q, y_0, τ_y, and τ_z using the LMFIT package in Python. The uncertainty in the emission rate can be estimated by evaluating how well the

https://doi.org/10.5194/egusphere-2026-51
Preprint. Discussion started: 20 January 2026

model fits the measured data (Shah et al., 2019) such that:

$$\Delta Q = Q\sqrt{\frac{\sum_j \left((q_{\mathrm{meas},j} - q_{\mathrm{mod},j})^2\right)}{\sum_j \left(q^2_{\mathrm{meas},j}\right)}} \tag{6}$$

This formulation for the uncertainty in Q accounts for both the variability in wind direction and the uncertainty in the positional data. We assume that uncertainties in the measurements of CH_4 concentration, wind speed, temperature, and pressure are negligible compared to the uncertainty in the model itself, and that the frequency of spatial sampling is sufficient to avoid any bias in flux estimation.

3 Results and Discussions

3.1 Comparing sensor response and wind measurements between UAV platforms

Both UAV-platforms were instrumented with an anemometer and CH_4 analyzer. The measured wind speed and direction for each system are corrected to account for the velocity of the UAV platform. Measured wind speeds from all four curtain flights are illustrated as a function of altitude in Fig. 3. The wind speed measurements are relatively consistent between the UAV platforms, and the wind conditions are similar for the far- and near-curtain flights. Both platforms show large wind speed variability at each altitude, with average standard deviations of $0.68\ \mathrm{ms}^{-1}$ and $0.64\ \mathrm{ms}^{-1}$ for UAV-MPI (CP-1 and CP-2) and UAV-NRCan (OP-1 and OP-2) at both curtains, respectively. Following Bolek et al. (2024), assuming a neutral boundary layer condition and logarithmic wind profile, we estimate the friction velocity u^* from the measured wind speed profile for each curtain (see Fig. 3). These values (u^*) are very similar across all flights, indicating comparable turbulence conditions. The uncertainty in u^* is smaller for UAV-NRCan compared to UAV-MPI, which can primarily be attributed to denser measurements in the vertical direction and faster movement of the UAV-NRCan. We correct UAV-MPI wind direction measurements for misalignment of the wind sensor relative to north, to yield mean wind directions of $189.8° \pm 10.8°$, $189.1° \pm 11.9°$, $188.0° \pm 7.9°$, and $189.0° \pm 7.9°$ for CP-1, CP-2, OP-1, and OP-2, respectively.

Figure 4 shows the CH_4 enhancements measured in each of the four curtain flights as a function of position in the curtain. A constant background CH_4 of 2.03 ppm and 2.06 ppm is removed from the measured concentrations for UAV-MPI and UAV-NRCan, respectively. The corresponding timeseries data is shown in the Appendix (Fig. B1). As UAV-MPI (CP-1 and CP-2) was piloted manually, the horizontal transect length and vertical spacing are less regular than for UAV-NRCan (OP-1 and OP-2), which used pre-programmed flights. In both cases, i.e. manual and pre-programmed flights, we ensured that the extents of the plume were captured by monitoring the sensors' data over a radio link in real-time. In addition, the lower transects in CP-2 were repeated after the initial curtain flight was complete (at around 15 m above takeoff), collecting additional data at the bottom of the curtain until the UAV-MPI battery was depleted.

The measured peak CH_4 enhancements for both OP curtains are 2-3 times larger than those measured in the CP curtains. The peak concentration enhancements measured in the far curtain flights CP-1 and OP-1 are 6.1 and 15.5 ppm, respectively. For the

https://doi.org/10.5194/egusphere-2026-51
Preprint. Discussion started: 20 January 2026

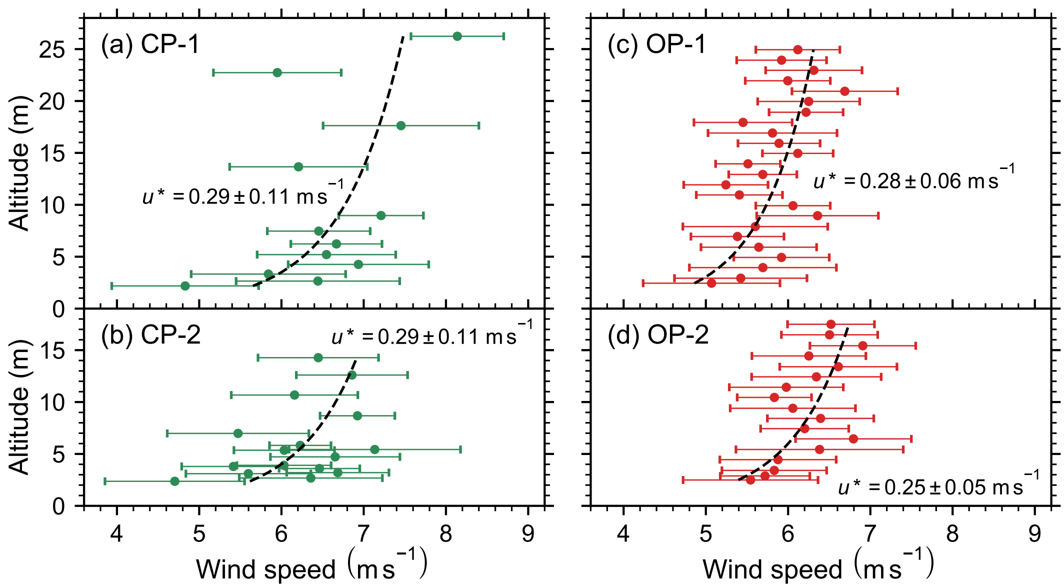

Figure 3. Measured wind speed and estimated friction velocities from (a, b) UAV-MPI and (c, d) UAV-NRCan. Closed circles represent mean wind speed at each altitude while standard deviations are represented as horizontal bars. The black dashed lines represent the logarithmic fitting. The flight ID is indicated in the top left corner for each flight (see Table 1).

near-curtain flights, the peak enhancements are 17.7 and 46.6 ppm for CP-2 and OP-2, respectively. The altitudes corresponding to the transects containing the peak concentrations are similar for both platforms: 5.2 m and 6.0 m for the far curtains CP-1 and OP-1, and 3.2 m and 3.4 m for the near curtains CP-2 and OP-2, respectively. Rather than indicating a substantial difference in the actual CH_4 concentration, the higher concentrations measured by the OP sensor are indicative of its much faster response time and lack of an enclosed sampling cell compared to the CP sensor. The limited pump speed and mixing within the enclosed sampling cell for the CP sensor result in an effective smoothing and broadening of the measured data. For this reason, distinct color scales are defined for the CP sensor curtains and the OP sensor curtains, capped at 16 ppm and 40 ppm for CP and OP, respectively.

To compare the performance of the closed path (CP; UAV-MPI) and open path (OP; UAV-NRCan) analyzers, we examine the transects with the peak concentration enhancement. The comparison is shown in Fig. 5(a) and (b) for far and near curtains, respectively. To facilitate comparison, the measured CH_4 concentration is plotted as a function of distance Δy relative to the peak along the y-axis (as defined in Fig. 2). The direction of travel along the transect for each UAV is indicated by an arrow in the legends of Fig. 5(a) and (b). In general, the signal from the OP analyzer shows much higher temporal resolution and associated fluctuations compared to CP, for which the measurements were much smoother. The width of the peak signal of both analyzers is more similar for the far curtain (OP-1 and CP-1) than for the near curtain. This is because the plume is more evenly dispersed at further distances from the source. Both sensors observe additional peaks on both sides of the central peak that are attributed to the plume meandering under turbulent conditions. However, the shape of the plume recorded by the CP sensor is

https://doi.org/10.5194/egusphere-2026-51
Preprint. Discussion started: 20 January 2026

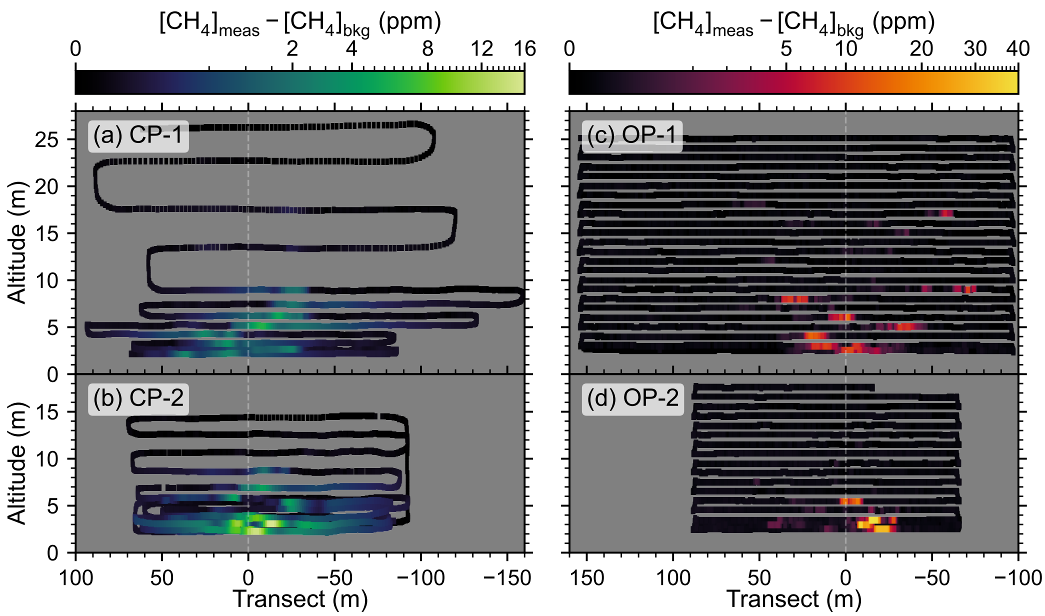

Figure 4. Measured methane concentrations after removing the background for the four curtain flights. (a, b) Curtains for the closed-path sensor at downwind distances of 163 m and 87 m, respectively. (c, d) Curtains for the open-path sensor at 149 m and 77 m downwind.

consistently asymmetrical with a gradual tail appearing after the UAV has crossed the plume (see Fig. 5 and Fig. B1). Apart from the smoothing and broadening of the measured data, the extended tail of CP measurement in the flight direction may also be attributed to (i) a slightly larger wind-incidence angle—supported by the shorter tail in the opposite flight direction, (ii) limited pump speed and/or friction within the tubing that prevents complete flush of the sampled air effectively.

https://doi.org/10.5194/egusphere-2026-51
Preprint. Discussion started: 20 January 2026

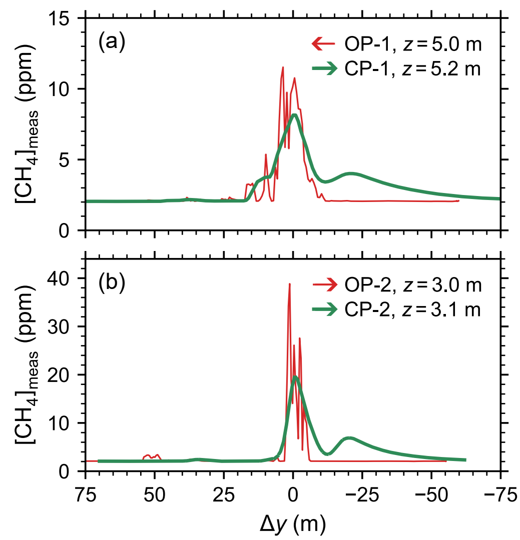

Figure 5. Comparison of methane concentrations measured by the closed- and open-path sensors over a single horizontal transect. (a) Horizontal transects measured at $z \approx 5$ m above ground-level for downwind distances of 163 m (CP-1) and 149 m (OP-1). (b) Transects at $z \approx 3$ m for 87 m (CP-2) and 77 m (OP-2). To facilitate comparison, the horizontal axis shows the distance Δy relative to the recorded peak. Arrows in the legends indicate the flight directions.

3.2 Emission flux quantification

3.2.1 Direct mass balance

The calculated transect integrated flux densities (i.e., $\int q_{\text{meas}} dy'$) for all curtains are illustrated in Figure 6. In all flights, the flux profiles converge to zero with increasing altitude, indicating that the plume extent in the vertical direction is fully captured. Using the DMB method, the emission rate of the seep is calculated to be 10.2 ± 4.6 kgCH$_4$ h^{-1} and 8.0 ± 4.3 kgCH$_4$ h^{-1} from CP-1 and CP-2, respectively. For OP-1 and OP-2, the calculated emission rates are 8.2 ± 3.5 kgCH$_4$ h^{-1} and 7.1 ± 3.4 kgCH$_4$ h^{-1}, respectively. For the far curtains (CP-1 and OP-1), minor enhancements are detected even above 15 m AGL, whereas for the near curtains (CP-2 and OP-2), no enhancement is captured above 10 m. Due to atmospheric turbulence, at some altitudes both platforms miss the plume, with only minimal enhancements observed at 5.5 m for CP-2, at 7 m for OP-1, and at 4.5 m for OP-2. As UAVs capture only the instantaneous plume, these events are unavoidable. However, dense vertical sampling and repeated measurements can minimize the impact of missing the plume; still, we estimate that missed plume sections contribute at most about 25% uncertainty (see Sec. 2.2.1) to the emission flux values reported here.

https://doi.org/10.5194/egusphere-2026-51
Preprint. Discussion started: 20 January 2026

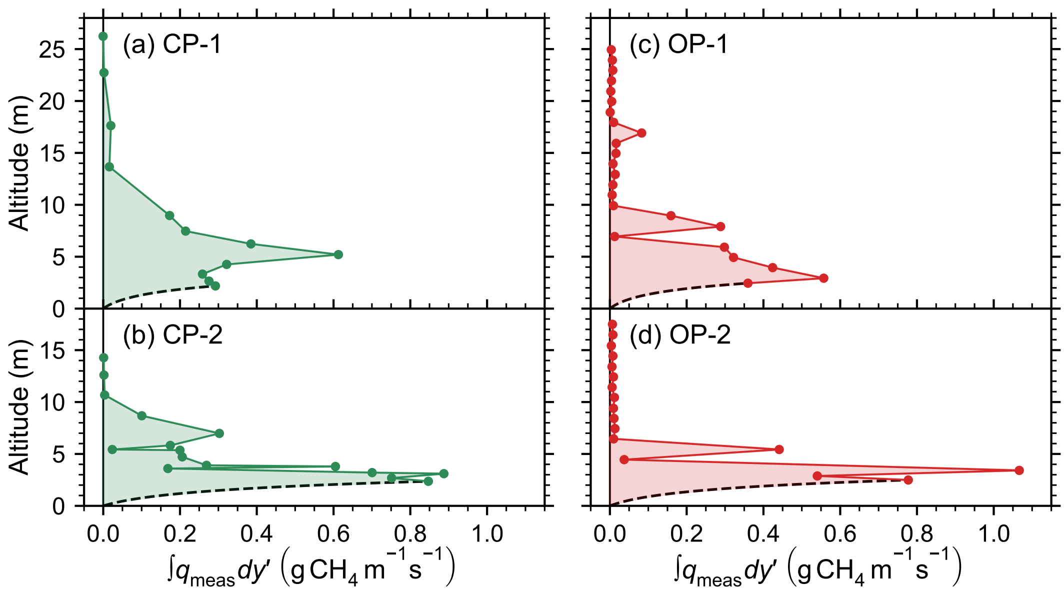

Figure 6. Calculated transect-integrated flux densities ($\int q_{\mathrm{meas}} dy'$) for each transect used in the DMB approach. The dashed lines indicate the logarithmic fitting that was employed to extrapolate the profile from the ground to the height of the first measurement transect.

The calculated emission rates for all curtains and platforms agree within their estimated uncertainties. The uncertainty ranges are about 45% of the estimated fluxes for all curtains, except for CP-2 (54%). The higher uncertainty range observed at CP-2 can be explained by the additional sampling of the lower transects after completing the curtain. This additional sampling close to the ground increases the variations in the measured concentration as plume dynamics are changing with time. Excluding the repeated transects, the emission rate is estimated to be $7.5 \pm 3.6\ \mathrm{kgCH_4\ h^{-1}}$, where the uncertainty is 48% of the estimated flux. This indicates that plume is time-variant and resampling a section of the curtain introduces additional uncertainties when applying the DMB method. As the additional transect measurements in CP-2 do not capture the full vertical extent of the plume, and therefore cannot be treated as an independent curtain. We combine the repeated transects close to the ground with the segment of the original curtain above 6 m to construct a new curtain (i.e., a second curtain patched with the repeated transects and above 6 m). The emission rate calculated from this new curtain is $8.6 \pm 4.1\ \mathrm{kgCH_4\ h^{-1}}$, which further supports the robustness of the methodology and data. Therefore, sampling the background concentration once while repeating plume-enhancement measurements close to the ground several times may be beneficial to optimize battery usage where on-site recharging is not feasible.

3.2.2 Cluster Kriging mass balance

We apply Cluster Kriging to interpolate the measured concentration fields for all curtains onto regular grids (see Fig. 7). Variograms are estimated using the Cressie-Hawkins method (Cressie and Hawkins, 1980) to fit the data with a model, as this

https://doi.org/10.5194/egusphere-2026-51
Preprint. Discussion started: 20 January 2026

estimator exhibits better performance compared to other available estimators (for more details please see (Mälicke, 2022)). We use a stable variogram model for the wind fields, but apply stable, exponential, and spherical models interchangeably for concentration fields whenever a better fit is observed. Here, to evaluate a better fit among the variograms we used RMSE (root mean square error) values.

Using the CKMB approach, emission rates for the UAV-MPI platform are calculated as $13.63 \pm 5.3\ \mathrm{kgCH_4\ h^{-1}}$ and $14.5 \pm 5.7\ \mathrm{kgCH_4\ h^{-1}}$. For UAV-NRCan, emission rates are estimated as $9.5 \pm 4.6\ \mathrm{kgCH_4\ h^{-1}}$ and $8.2 \pm 4.6\ \mathrm{kgCH_4\ h^{-1}}$ for OP-1 and -2, respectively. As expected, the plume that is captured by the CP sensor appears wider than the OP sensor, especially when comparing curtains CP-2 and OP-2, which are nearer to the source (Fig. 7(b) and (d)). While Morales et al. (2022) previously indicated that CKMB provides better estimates at downwind distances shorter than 75 m— a threshold exceeded for all of the curtains in this study—that threshold assumed UAVs could not fully map plumes extending above 10 m. In this work, however, both platforms flew up to 25 m altitude (Fig. 4), successfully capturing the full vertical extent of the plume. Here, UAV-NRCan flew dense vertical transects with higher flight speed, whereas UAV-MPI was flying at a slower speed and the transect spacing was adjusted at higher altitudes to accommodate the limited battery life while still sampling the full vertical extent of the plume.

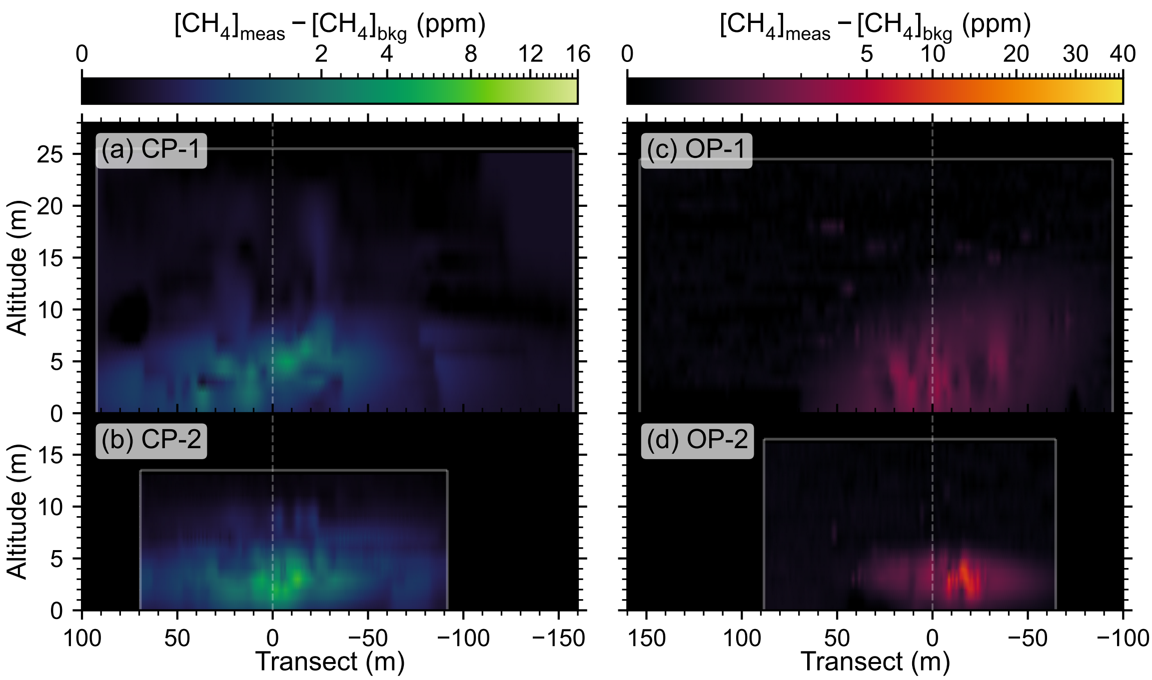

Figure 7. Kriged CH_4 enhancement fields from UAV-MPI for flights (a) CP-1 and (b) CP-2 and from UAV-NRCan for flights (c) OP-1 and (d) OP-2. The measured curtain extents are illustrated with boxes indicated by white lines, and the center of the curtain is indicated with a white vertical dashed line.

https://doi.org/10.5194/egusphere-2026-51
Preprint. Discussion started: 20 January 2026

3.2.3 Gaussian plume inversion

The near-field Gaussian plume inversion (GPI) is applied by fitting Eq. 4 to the measured flux densities q_{meas}, calculated according to Eq. 5 and shown in the appendix (Fig. C1). The GPI allows the modeled plume to be reconstructed in three dimensions. Therefore, for each measurement platform, we fit the measured data for one curtain but use the resulting plume model to reconstruct both curtains, for illustration purposes. The fit parameters for each curtain are summarized in Table 2. The modeled plumes obtained by fitting the far curtains (CP-1 and OP-1) are shown in Fig. 8, and the plumes obtained by fitting the near curtains (CP-2 and OP-2) are shown in Fig. 9.

Table 2. Fitting parameters for Eq. 4 obtained using the near-field GPI.

Flight ID	y_0 (m)	τ_y	τ_z	Q $\left(\mathrm{kgCH_4h^{-1}}\right)$	ΔQ $\left(\mathrm{kgCH_4h^{-1}}\right)$
CP-1	-4.90	0.14	0.05	14.1	10.5
CP-2	-1.56	0.22	0.02	16.2	12.4
OP-1	6.60	0.11	0.03	10.9	9.7
OP-2	-16.78	0.07	0.03	16.0	13.4

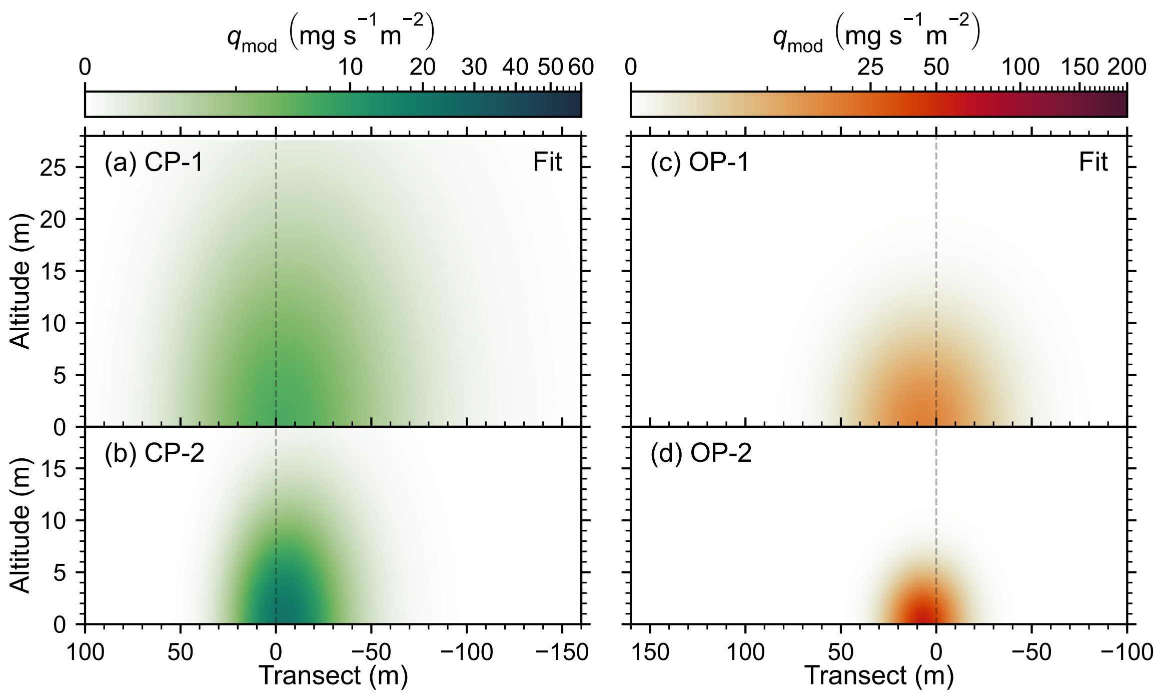

Figure 8. Modeled flux densities obtained from applying the near-field GPI to the far flux curtains (CP-1 and OP-1). The model results are shown for all four flux curtains, though the model parameters were obtained using only CP-1 and OP-1, indicated as Fit.

https://doi.org/10.5194/egusphere-2026-51
Preprint. Discussion started: 20 January 2026

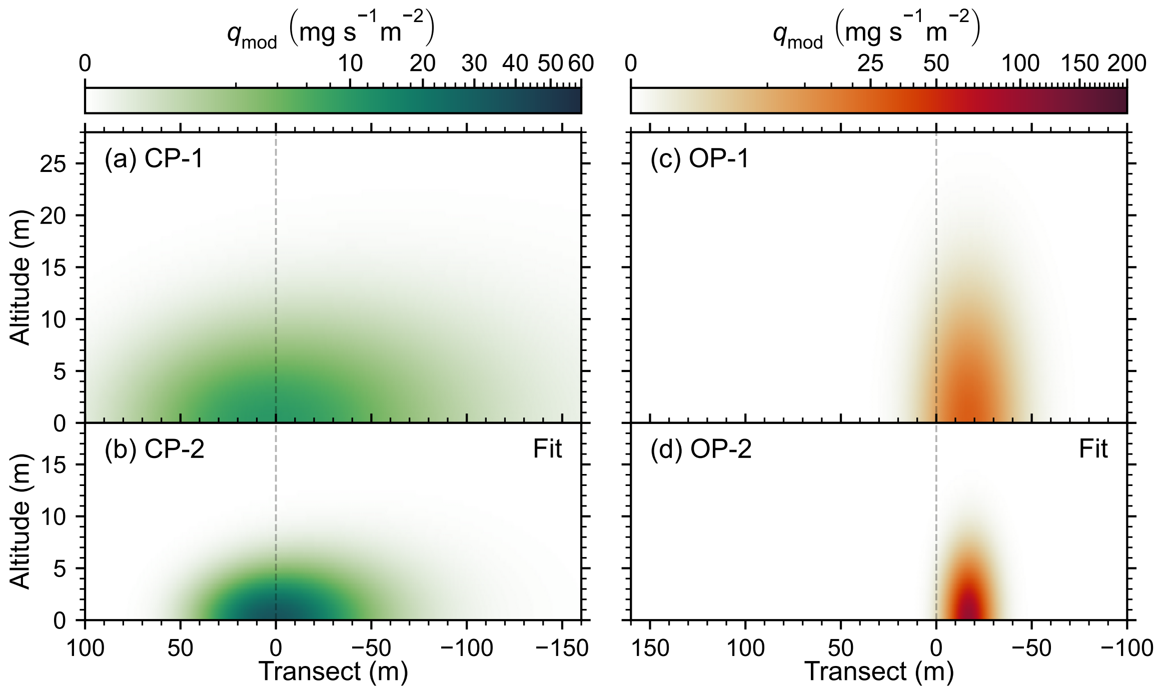

Figure 9. Modeled flux densities obtained from applying the near-field GPI to the near flux curtains (CP-2 and OP-2). The model results are shown for all four flux curtains, though the model parameters were obtained using only CP-2 and OP-2, indicated as Fit.

In all cases, the source height is fixed at $h = 0$ and the remaining parameters are allowed to vary. We expected the plume to be centered close to $y_0 = 0$, in line with the prevailing wind direction. However, turbulence and variability in the instantaneous wind direction lead to non-zero values for y_0, ranging from -16.78 to +6.60 m. The deviations in y_0 are larger for the OP sensor compared to the CP sensor.

When fitting the far curtains (CP-1 and OP-1, Fig. 8), the shape of the modeled plume is similar for both the OP and CP systems, though the result obtained for the CP sensor appears more dispersed, attributed to the CP sensor's signal broadening effect. The results obtained when fitting the near curtains (CP-2 and OP-2, Fig. 9) show substantial differences in the shape of the modeled plume, with much broader apparent horizontal dispersion (τ_y) for CP-2 compared to OP-2. In this case, at just ~80 m downwind of the source, the plume has had little opportunity to disperse and is highly influenced by turbulence and local eddies. At this distance, the difference in response of the CP and OP sensors is pronounced. Furthermore, we see that the perceived shape of the emission plume is strongly influenced by the response of the sensor. This suggests that application of prescriptive dispersion models that define the expected shape of a plume based on average local atmospheric conditions without accounting for the sensor response and the measurement duration, such as the Pasquill Stability Classes (Pasquill, 1961), are ill-suited for near-field measurements obtained by UAVs. However, in comparing Fig. 8 and Fig. 9, it is apparent that the capacity of the near-field Gaussian plume formalism to reproduce the shape of the plume in three dimensions remains

https://doi.org/10.5194/egusphere-2026-51
Preprint. Discussion started: 20 January 2026

limited, at least for downwind distances in the 80 to 160 m range with short observation times and atmospheric conditions similar to those presented here.

Comparing the emission flux estimates reported in Table 2, all values fall in the range from 10.9 to 16.2 $\mathrm{kgCH_4h^{-1}}$, in agreement within their respective uncertainties. The large error bounds, ranging from 74% to 89% of the corresponding flux estimates, are due to the large residuals between the Gaussian plume model and the measured data, indicating the Gaussian plume model does not adequately represent the measurement data. Though agreeing well within the prescribed uncertainty, we note that the difference between the estimated flux rates for the far and near curtains is smaller for the CP sensor compared to the OP sensor. We attribute this effect to the more gradual response of the CP sensor, which more closely resembles a smoothly varying Gaussian plume than the OP sensor.

3.3 Comparison between flux estimates

The estimated emission rates from all of these methods are provided in Fig. 10. Overall, the estimated emission rates from all UAV platforms and methods used in this study overlap within their respective uncertainty ranges. The application of DMB is straightforward and produces the most consistent results across curtains and UAV platforms. However, adequate sampling density is essential, particularly in the vertical direction. Sparse sampling in the vertical direction can lead to large uncertainties and underestimation of the emission flux, especially when the plume center is missed (estimated to be about 25%). The uncertainties associated with extrapolation between the ground and the first measuring height, and the linear interpolations between transects, are largely unknown and may be underestimated in this study. Further investigation is needed to quantify these uncertainties.

In the CKMB emission rate quantification method, the interpolation uncertainty can be directly and conveniently quantified using covariance matrices. The CKMB method provides excellent agreement in the emission rate estimates when comparing the far and near curtains for each UAV platform individually. However, the variation between the platforms is greatest for CKMB compared to the other quantification methods. This is likely due to sensor response times and differences in flight execution: the OP platform utilized autonomous flight paths (resulting in regular sampling spacing), whereas the CP platform was manually piloted (resulting in irregular sampling spacing). Dense, autonomous flight patterns may be preferable to improve the consistency of flux estimates. Compared to DMB, the CKMB method is more complicated to apply and computationally more demanding as the curtain area increases. Additionally, fitting a variogram to the measured data usually requires optimizing the variance and length scales, which may not always converge.

The near-field Gaussian Plume Inversion (GPI) generates larger emission rate estimates than DMB and CKMB for all flux curtains except for CP-2, which fell between the corresponding mass balance estimates. However, estimations from CKMB and GPI methods for the UAV-MPI samples were very similar, particularly for the near curtain. Because both methods (CKMB and GPI) tend to smooth the observed methane enhancements and widen the modeled plume extent, both vertically and horizontally, they typically yield larger emission rate estimates compared to DMB.

The difference between the DMB and CKMB flux estimates is larger for the UAV-MPI, 25% for CP-1 and 45% for CP-2, whereas the differences for UAV-NRCan are about 15% for both OP-1 and -2. The observed differences between applied

https://doi.org/10.5194/egusphere-2026-51
Preprint. Discussion started: 20 January 2026

interpolation schemes in mass balance approaches can be due to the fact that UAVs sample instantaneous plume dynamics rather than a static representation of the plume; hence, the variations in plume dynamics can lead to these differences in interpolation and emission rate estimates. These differences can also be partly attributed to the different flight strategies. The curtains flown by UAV-NRCan (OP) are denser and the data is more uniform than the UAV-MPI curtains (CP). This difference is most likely reflected in the interpolation algorithms, either Kriging or linear interpolation, producing larger differences between these two methods for CP-1 and -2. In addition, tailing towards the flight direction in CP data might be another factor that impacts the interpolation algorithms and causes these discrepancies between the two methods. Even in OP-based flux estimations, where no tailing and more uniform sampling were achieved, the 15% difference observed between these two methods can mainly be attributed to different interpolation algorithms. With non-uniform sampling, the difference between interpolation schemes is expected to increase, which was observed in CP-based flux calculations.

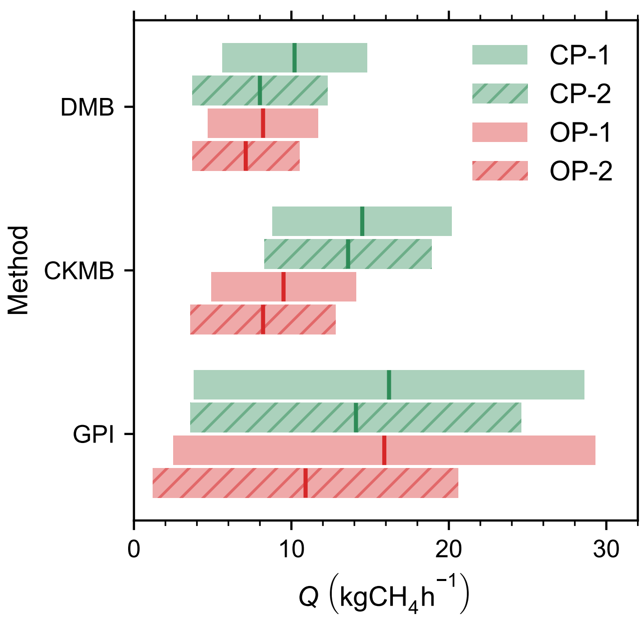

Figure 10. Comparison of all flux estimations (Q) from different models and UAV platforms. Here, DMB, CKMB, and GPI denote Direct Mass Balance, Cluster Kriging Mass Balance, and Gaussian Plume Inversion approaches. Far curtains OP-1 and CP-1 are represented as solid red and green bars and near curtains OP-2 and CP-2 are represented with hashed red and green bars, respectively.

4 Conclusions

Atmospheric research using UAV-based measurement methodologies and associated instruments is still in its early stages and their full potential remains to be determined. To that end, here we evaluate several point source emission rate quantification methodologies using two UAV platforms equipped with methane analyzers, one open path (OP) and the other closed path (CP). Each platform conducted two curtain flights at two downwind distances, near curtain (∼80 m) and far curtain (∼150

https://doi.org/10.5194/egusphere-2026-51
Preprint. Discussion started: 20 January 2026

m). Although we use different anemometers on each platform, the wind measurements are consistent between the two UAV platforms, with close prediction (with about 15% discrepancy) of friction velocities. Comparison between the methane concentration measurements for both UAV platforms shows that the OP analyzer often records sharper and larger CH_4 peaks, while the peaks are much smoother and damped for the CP analyzer. The OP analyzer may be preferable for plume tracking due to its higher sampling rate and lower latency compared to the CP analyzer. However, plume morphologies are discrete due to sharp peaks in OP, and rather smooth in the CP.

If UAV-based wind measurements are available, mass balance approaches (CKMB and DMB) to quantification should be preferred over the GPI because they reduce the number of assumptions involved in the calculations. Nevertheless, GPI method can become practical whenever an on-board wind measurement is not available although this may lead to higher uncertainties. Provided that the full extent of the plume is captured along both the crosswind and vertical axes, both of the mass balance methods are expected to yield similar emission rate estimations. With dense sampling along vertical and horizontal directions, the DMB method may be a better alternative, as it is straightforward to apply compared to CKMB. Overall, the UAV-based methodologies presented in this study enable quantification of the emission rates from hard-to-access methane point sources that would otherwise be difficult to quantify.

Despite the differences in equipment and analysis methodologies used here and their associated uncertainties, the present work estimates that the methane emission rate of the investigated seep is in the range of 7.1 kgCH_4/h to 16.2 kgCH_4/h with an average value of $11.4 \pm 6.8\ \mathrm{kgCH_4\ h^{-1}}$. Although this value only represents emissions during the active-layer thaw conditions, and does not reflect seasonal variations in emission rates, this average emission rate is significantly higher than biogenic sources. When compared to maximum daily biogenic CH_4 fluxes from permafrost landscapes (ranges approximately between $1.6-5\,\mathrm{mg\,m^{-2}\,h^{-1}}$, Friborg et al. (2000); Skeeter et al. (2022)), emissions from this point source are equivalent to biogenic emissions from a minimum area of 2.2 km^2, pointing to the importance of identification, quantification, and inclusion of such emission sources in Earth-System models.

Code and data availability. The code and data used in this manuscript will be made publicly available upon acceptance.

Appendix A: Custom temperature controller for Aeris Strato

The Aeris Strato CH_4 analyzer used on the UAV-MPI platform was customized with a thermally controlled enclosure to stabilize the cell temperature and reduce signal drift (see Fig. A1 (a)). A thermal enclosure surrounding the measuring cell was added, including peltier elements for heating/cooling to keep the temperature within that enclosure stable (at 41 °C) using a temperature controller (TEC-1091, Meerstetter Engineering GmbH). This controller unit was directly powered up by the analyzer board, minimizing system weight and complexity. We tested the performance of the analyzer against a calibration gas in a climate chamber. The calibration gas was routed through a coil-shaped steel tubing to equilibrate the gas temperature with the climate chamber temperature as much as possible.

https://doi.org/10.5194/egusphere-2026-51
Preprint. Discussion started: 20 January 2026

Prior to testing the impact of the temperature controller, we observed large temperature fluctuations (±10) within the analyzer cell under relatively stable conditions (see Fig. A1 (b)). The TEC OFF test was conducted between 13:50 to 14:10 (black dashed lines in Fig. A1 (b)). Although the climate chamber temperature was set to cycle between 10 - 15 °C every minute for about 20 minutes, the analyzer cell temperature was increasing throughout the test. This increase can be attributed to the low cooling efficiency of the thermally controlled enclosure and self-heating of the analyzer's cell. Later, the temperature controller was turned on (TEC ON, 14:12) and the instrument was allowed to warm up for about 30 minutes until the cell temperature was stabilized around 41 °C. The TEC ON test was conducted (red dashed lines in Fig. A1 (b)) under the same climate chamber setup as TEC OFF test. The standard deviation of the cell temperature during TEC ON was calculated as 0.01 °C, whereas this was 1.62 °C during TEC OFF test. This was also reflected in CH_4 measurements (see Fig. A1 (c)), the standard deviation during TEC OFF was 5.48 ppb (IQR 10.5 ppb), whereas during TEC ON this was 1.45 ppb (IQR 1.94 ppb). The improvement of the analyzer was also shown with Allan-Werle-plots (Fig. A1 (d)). The instrument noise for longer averaging times is much smaller with the temperature controller unit compared to without one.

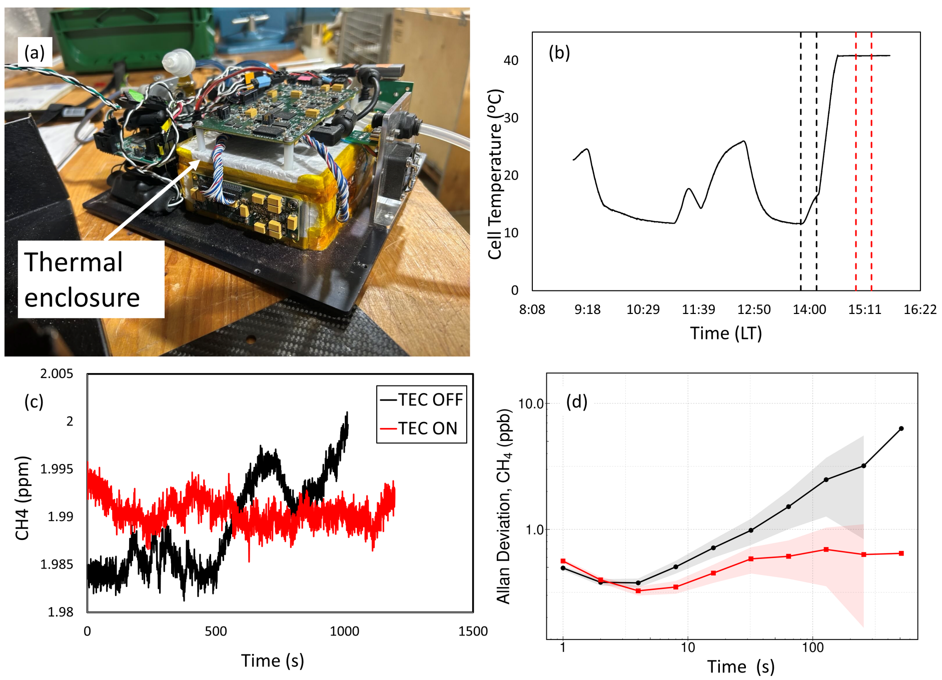

Figure A1. Customized Aeris Strato analyzer (a) showing thermally controlled enclosure wrapped around the measuring cell (b) recorded cell temperature of the analyzer during the climate chamber test, (c) measured CH_4 concentration with and without temperature controller (d) Allan-Werle=plots of both conditions. Here, red colors represent when the temperature controller unit was on (TEC ON) while black colors represent when the temperature controller was off (TEC OFF).

https://doi.org/10.5194/egusphere-2026-51
Preprint. Discussion started: 20 January 2026

Appendix B: Timeseries data for measured flux curtains

Figure B1 shows the measured methane mixing ratios for all curtains from both UAV platforms.

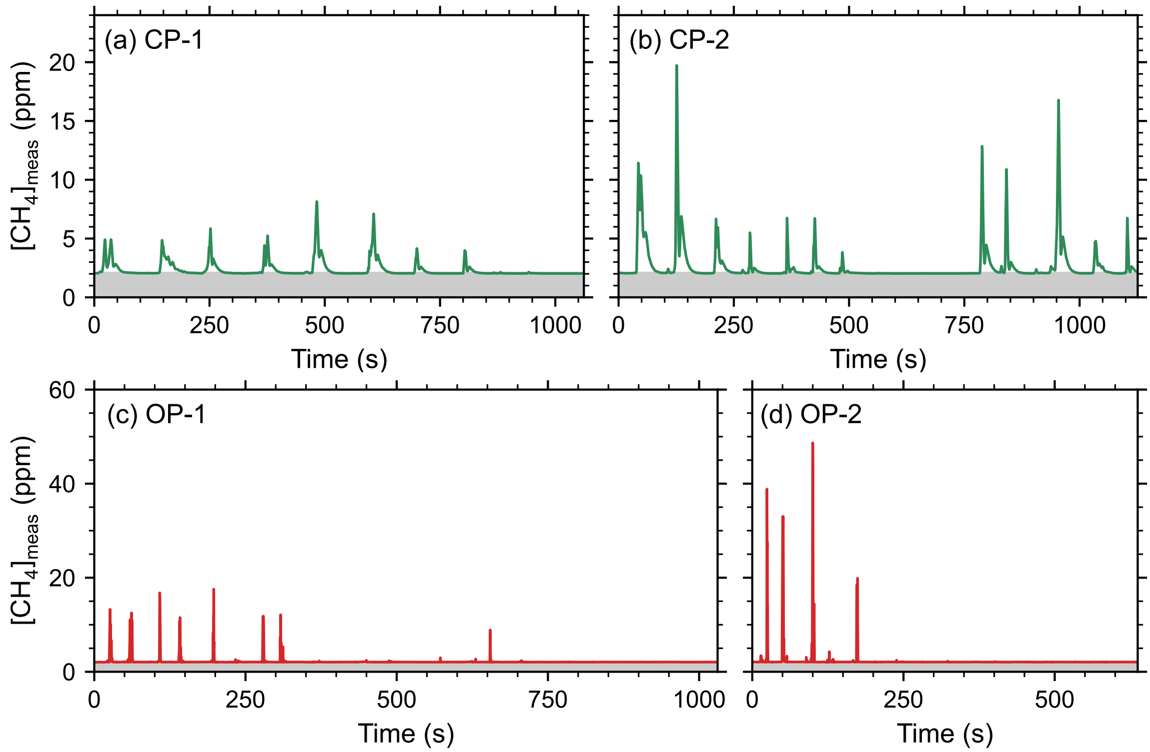

Figure B1. Measured methane concentration timeseries for the four curtain flights, labeled CP-1, CP-2, OP-1, and OP-2. The shaded regions indicate the background methane concentration, recorded as 2.03 ppm for the closed-path sensor (a,b) and 2.06 ppm for the open-path sensor (c,d).

Appendix C: Flux densities used for Gaussian plume inversion

The calculated methane flux densities (q_{meas}) for all curtains from both UAV platforms are shown in Fig. C1.

https://doi.org/10.5194/egusphere-2026-51
Preprint. Discussion started: 20 January 2026

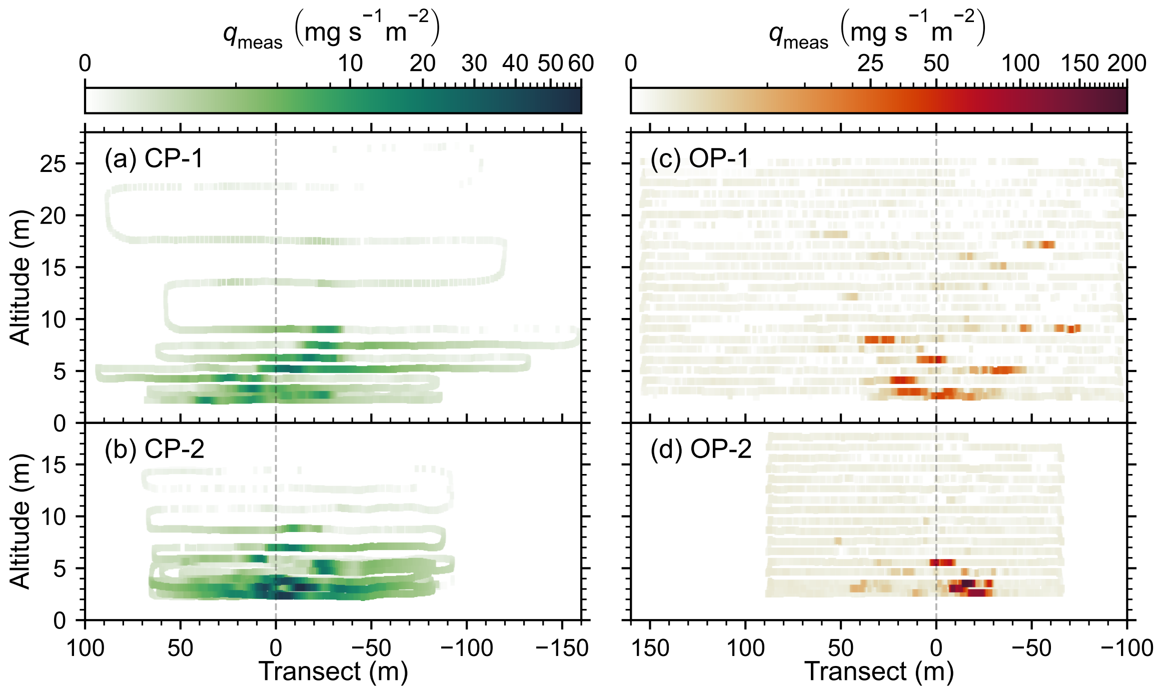

Figure C1. Methane flux densities calculated from equation 5 (a, b). Flux density for the closed-path sensor at downwind distances of 163 m and 87 m, respectively. (c, d) Flux density for the open-path sensor at 149 m and 77 m downwind.

Author contributions. AB, MNB, and JNO conceptualized the manuscript. PM developed the opportunity for field experimentation and coordinated the field logistics and research licensing. AB, MNB, RM, JNO, and JS designed and conducted field experiments. AB, MNB, and JNO performed the formal analysis and wrote the original draft. JNO, PM, MH, and MG acquired funding, provided supervision, and reviewed the manuscript.

Competing interests. The corresponding author has declared that none of the authors has any competing interests

Acknowledgements. This study was supported by the European Research Council (ERC) under the European Union's Horizon 2020 research and innovation program (grant agreement no. 951288, Q-Arctic), by Natural Resources Canada's (NRCan) Office of Energy Research and Development (grant no. NRC-23-137 to JNO). NRCan provided additional financial support to the study through OERD to the Geological Survey of Canada's (GSC) GeoEnergy program and through GSC's Natural Hazards Climate Change Geoscience program. Logistical

https://doi.org/10.5194/egusphere-2026-51
Preprint. Discussion started: 20 January 2026

support was provided by NRCan's Polar Continental Shelf Program (project no. 003-25) and Aurora College's Western Arctic Research Centre. Wildlife monitoring was provided by Johnny Aviugana of the Inuvik Hunters and Trappers Committee. Fieldwork was conducted under Northwest Territories Scientific Research License no. 17696. This work used resources of the Deutsches Klimarechenzentrum (DKRZ) granted by its Scientific Steering Committee (WLA) under project ID bm1236. We thank David Ho for his thoughtful comments and suggestions. We also thank MPI-BGC service group for their help in implementing the thermally controlled enclosure.

https://doi.org/10.5194/egusphere-2026-51
Preprint. Discussion started: 20 January 2026

References

Andersen, T., Scheeren, B., Peters, W., and Chen, H.: A UAV-based active AirCore system for measurements of greenhouse gases, Atmospheric Measurement Techniques, 11, 2683–2699, https://doi.org/10.5194/amt-11-2683-2018, 2018.

Andersen, T., Vinkovic, K., de Vries, M., Kers, B., Necki, J., Swolkien, J., Roiger, A., Peters, W., and Chen, H.: Quantifying methane emissions from coal mining ventilation shafts using an unmanned aerial vehicle (UAV)-based active AirCore system, Atmospheric Environment: X, 12, 100 135, https://doi.org/https://doi.org/10.1016/j.aeaoa.2021.100135, 2021.

Andersen, T., Zhao, Z., de Vries, M., Necki, J., Swolkien, J., Menoud, M., Röckmann, T., Roiger, A., Fix, A., Peters, W., et al.: Local-to-regional methane emissions from the Upper Silesian Coal Basin (USCB) quantified using UAV-based atmospheric measurements, Atmospheric Chemistry and Physics, 23, 5191–5216, https://doi.org/https://doi.org/10.5194/acp-23-5191-2023, 2023.

Ayasse, A. K., Thorpe, A. K., Roberts, D. A., Funk, C. C., Dennison, P. E., Frankenberg, C., Steffke, A., and Aubrey, A. D.: Evaluating the effects of surface properties on methane retrievals using a synthetic airborne visible/infrared imaging spectrometer next generation (AVIRIS-NG) image, Remote sensing of environment, 215, 386–397, 2018.

Baskaran, L., Elder, C., Bloom, A. A., Ma, S., Thompson, D., and Miller, C. E.: Geomorphological patterns of remotely sensed methane hot spots in the Mackenzie Delta, Canada, Environmental Research Letters, 17, 015 009, 2022.

Bolek, A. and Testik, F.: Atmospheric Boundary Layer Turbulence Measurements Using sUAS with Neural Network Application, in: AIAA AVIATION 2022 Forum, p. 4112, 2022.

Bolek, A., Heimann, M., and Göckede, M.: UAV-based in situ measurements of CO_2 and CH_4 fluxes over complex natural ecosystems, Atmospheric Measurement Techniques, 17, 5619–5636, https://doi.org/10.5194/amt-17-5619-2024, 2024.

Bonne, J.-L., Donnat, L., Albora, G., Burgalat, J., Chauvin, N., Combaz, D., Cousin, J., Decarpenterie, T., Duclaux, O., Galas, N., Juery, C., Parent, F., Pineau, F., Maunoury, A., Ventre, O., Bénassy, M.-F., and Joly, L.: A simultaneous CH4 and CO2 flux quantification method for industrial site emissions from in-situ concentration measurements on-board an Unmanned Aircraft Vehicle, Atmospheric Measurement Techniques Discussions, pp. 1–27, https://doi.org/10.5194/amt-2022-334, 2023.

Bonne, J.-L., Donnat, L., Albora, G., Burgalat, J., Chauvin, N., Combaz, D., Cousin, J., Decarpenterie, T., Duclaux, O., Dumelié, N., Galas, N., Juery, C., Parent, F., Pineau, F., Maunoury, A., Ventre, O., Bénassy, M.-F., and Joly, L.: A measurement system for CO_2 and CH_4 emissions quantification of industrial sites using a new in situ concentration sensor operated on board uncrewed aircraft vehicles, Atmospheric Measurement Techniques, 17, 4471–4491, https://doi.org/10.5194/amt-17-4471-2024, 2024.

Borchardt, J., Harris, S. J., Hacker, J. M., Lunt, M., Krautwurst, S., Bai, M., Bösch, H., Bovensmann, H., Burrows, J. P., Chakravarty, S., Field, R. A., Gerilowski, K., Huhs, O., Junkermann, W., Kelly, B. F. J., Kumm, M., Lieff, W., McGrath, A., Murphy, A., Schindewolf, J., and Thoböll, J.: Insights into Elevated Methane Emissions from an Australian Open-Cut Coal Mine Using Two Independent Airborne Techniques, Environmental Science & Technology Letters, 12, 397–404, https://doi.org/10.1021/acs.estlett.4c01063, 2025.

Burn, C. R. and Kokelj, S. V.: The environment and permafrost of the Mackenzie Delta area, Permafrost and Periglacial Processes, 20, 83–105, https://doi.org/https://doi.org/10.1002/ppp.655, 2009.

Burn, C. R., Mackay, J. R., and Kokelj, S. V.: The thermal regime of permafrost and its susceptibility to degradation in upland terrain near Inuvik, N.W.T., Permafrost and Periglacial Processes, 20, 221–227, https://doi.org/https://doi.org/10.1002/ppp.649, 2009.

Cressie, N. and Hawkins, D.: Robust estimation of the variogram: I, Mathematical Geology, 12, 115–125, https://doi.org/10.1007/BF01035243, 1980.

Dallimore, S. R., Lapham, L. L., Côté, M. M., Bowen, R., MacLeod, R., McIntosh Marcek, H. A., Wheat, C. G., and Collett, T. S.: Source, Migration Pathways, and Atmospheric Release of Geologic Methane Associated With the Complex Permafrost Regimes of the Outer Mackenzie River Delta, Northwest Territories, Canada, Journal of Geophysical Research: Earth Surface, 129, e2023JF007 515, https://doi.org/https://doi.org/10.1029/2023JF007515, e2023JF007515 2023JF007515, 2024.

Detto, M., Verfaillie, J., Anderson, F., Xu, L., and Baldocchi, D.: Comparing laser-based open- and closed-path gas analyzers to measure methane fluxes using the eddy covariance method, Agricultural and Forest Meteorology, 151, 1312–1324, https://doi.org/https://doi.org/10.1016/j.agrformet.2011.05.014, 2011.

Elder, C., Kohnert, K., Serafimovich, A., Thorpe, A., Thompson, D., Sachs, T., and Miller, C.: Broad spatial comparison of methane emission patterns in the Mackenzie Delta, NWT using complimentary airborne eddy covariance and hyperspectral visible/infrared imaging spectroscopy, in: EGU General Assembly Conference Abstracts, p. 12512, 2019.

Fiehn, A., Kostinek, J., Eckl, M., Klausner, T., Gałkowski, M., Chen, J., Gerbig, C., Röckmann, T., Maazallahi, H., Schmidt, M., Korbeń, P., Neçki, J., Jagoda, P., Wildmann, N., Mallaun, C., Bun, R., Nickl, A.-L., Jöckel, P., Fix, A., and Roiger, A.: Estimating CH_4, CO_2 and CO emissions from coal mining and industrial activities in the Upper Silesian Coal Basin using an aircraft-based mass balance approach, Atmospheric Chemistry and Physics, 20, 12 675–12 695, https://doi.org/10.5194/acp-20-12675-2020, 2020.

Friborg, T., Christensen, T. R., Hansen, B. U., Nordstroem, C., and Soegaard, H.: Trace gas exchange in a high-Arctic valley: 2. Landscape CH4 fluxes measured and modeled using eddy correlation data, Global Biogeochemical Cycles, 14, 715–723, https://doi.org/https://doi.org/10.1029/1999GB001136, 2000.

Gålfalk, M., Nilsson Påledal, S., and Bastviken, D.: Sensitive Drone Mapping of Methane Emissions without the Need for Supplementary Ground-Based Measurements, ACS Earth and Space Chemistry, 5, 2668–2676, https://doi.org/10.1021/acsearthspacechem.1c00106, 2021.

Karion, A., Sweeney, C., Pétron, G., Frost, G., Michael Hardesty, R., Kofler, J., Miller, B. R., Newberger, T., Wolter, S., Banta, R., Brewer, A., Dlugokencky, E., Lang, P., Montzka, S. A., Schnell, R., Tans, P., Trainer, M., Zamora, R., and Conley, S.: Methane emissions estimate from airborne measurements over a western United States natural gas field, Geophysical Research Letters, 40, 4393–4397, https://doi.org/https://doi.org/10.1002/grl.50811, 2013.

Kohnert, K., Serafimovich, A., Metzger, S., Hartmann, J., and Sachs, T.: Strong geologic methane emissions from discontinuous terrestrial permafrost in the Mackenzie Delta, Canada, Scientific Reports, 7, 5828, https://doi.org/10.1038/s41598-017-05783-2, 2017.

Kunz, M., Lavric, J., Gerbig, C., Tans, P., Neff, D., Hummelgärd, C., Martin, H., Rödjegärd, H., Wrenger, B., and Heimann, M.: COCAP: A carbon dioxide analyser for small unmanned aircraft systems, Atmospheric Measurement Techniques, 11, 1833–1849, https://doi.org/10.5194/amt-11-1833-2018, 2018.

Kunz, M., Lavric, J. V., Gasche, R., Gerbig, C., Grant, R. H., Koch, F. T., Schumacher, M., Wolf, B., and Zeeman, M.: Surface flux estimates derived from UAS-based mole fraction measurements by means of a nocturnal boundary layer budget approach, Atmospheric Measurement Techniques, 13, 1671–1692, https://doi.org/10.5194/amt-13-1671-2020, 2020.

Mälicke, M.: SciKit-GStat 1.0: a SciPy-flavored geostatistical variogram estimation toolbox written in Python, Geoscientific Model Development, 15, 2505–2532, https://doi.org/10.5194/gmd-15-2505-2022, 2022.

Miner, K. R., Turetsky, M. R., Malina, E., Bartsch, A., Tamminen, J., McGuire, A. D., Fix, A., Sweeney, C., Elder, C. D., and Miller, C. E.: Permafrost carbon emissions in a changing Arctic, Nature Reviews Earth Environment, 3, 55–67, https://doi.org/https://doi.org/10.1038/s43017-021-00230-3, 2022.

https://doi.org/10.5194/egusphere-2026-51
Preprint. Discussion started: 20 January 2026

Mohammadloo, T. H., Jones, M., van de Kerkhof, B., Dawson, K., Smith, B. J., Conley, S., Corbett, A., and IJzermans, R.: Quantitative estimate of several sources of uncertainty in drone-based methane emission measurements, Atmospheric Measurement Techniques, 18, 1301–1324, https://doi.org/10.5194/amt-18-1301-2025, 2025.

Morales, R., Ravelid, J., Vinkovic, K., Korbeń, P., Tuzson, B., Emmenegger, L., Chen, H., Schmidt, M., Humbel, S., and Brunner, D.: Controlled-release experiment to investigate uncertainties in UAV-based emission quantification for methane point sources, Atmospheric Measurement Techniques, 15, 2177–2198, https://doi.org/10.5194/amt-15-2177-2022, 2022.

Müller, S., Schüler, L., Zech, A., and Heße, F.: `GSTools` v1.3: a toolbox for geostatistical modelling in Python, Geoscientific Model Development, 15, 3161–3182, https://doi.org/10.5194/gmd-15-3161-2022, 2022.

Pasquill, F.: The estimation of the dispersion of windborne material, Meteorological Magazine, 90, 33–49, 1961.

Rantanen, M., Karpechko, A. Y., Lipponen, A., Nordling, K., Hyvärinen, O., Ruosteenoja, K., Vihma, T., and Laaksonen, A.: The Arctic has warmed nearly four times faster than the globe since 1979, Communications Earth Environment, 3, 168, https://doi.org/https://doi.org/10.1038/s43247-022-00498-3, 2022.

Scheller, J. H., Mastepanov, M., and Christensen, T. R.: Toward UAV-based methane emission mapping of Arctic terrestrial ecosystems, Science of the Total Environment, 819, https://doi.org/10.1016/j.scitotenv.2022.153161, 2022.

Scheutz, C., Knudsen, J., Vechi, N., and Knudsen, J.: Validation and demonstration of a drone-based method for quantifying fugitive methane emissions, Journal of Environmental Management, 373, 123 467, https://doi.org/https://doi.org/10.1016/j.jenvman.2024.123467, 2025.

Shah, A., Allen, G., Pitt, J. R., Ricketts, H., Williams, P. I., Helmore, J., Finlayson, A., Robinson, R., Kabbabe, K., Hollingsworth, P., Rees-White, T. C., Beaven, R., Scheutz, C., and Bourn, M.: A Near-Field Gaussian Plume Inversion Flux Quantification Method, Applied to Unmanned Aerial Vehicle Sampling, Atmosphere, 10, https://www.mdpi.com/2073-4433/10/7/396, 2019.

Shah, A., Pitt, J. R., Ricketts, H., Leen, J. B., Williams, P. I., Kabbabe, K., Gallagher, M. W., and Allen, G.: Testing the near-field Gaussian plume inversion flux quantification technique using unmanned aerial vehicle sampling, Atmospheric Measurement Techniques, 13, 1467–1484, https://doi.org/10.5194/amt-13-1467-2020, 2020.

Shaw, J. T., Shah, A., Yong, H., and Allen, G.: Methods for quantifying methane emissions using unmanned aerial vehicles: A review, Philosophical Transactions of the Royal Society A: Mathematical, Physical and Engineering Sciences, 379, https://doi.org/10.1098/rsta.2020.0450, 2021.

Skeeter, J., Christen, A., and Henry, G. H.: Controls on carbon dioxide and methane fluxes from a low-center polygonal peatland in the Mackenzie River Delta, Northwest Territories, Arctic Science, 8, 471–497, https://doi.org/10.1139/as-2021-0034, 2022.

Takriti, M., Wynn, P. M., Elias, D. M., Ward, S. E., Oakley, S., and McNamara, N. P.: Mobile methane measurements: Effects of instrument specifications on data interpretation, reproducibility, and isotopic precision, Atmospheric Environment, 246, 118 067, https://doi.org/https://doi.org/10.1016/j.atmosenv.2020.118067, 2021.

Thielicke, W., Hübert, W., Müller, U., Eggert, M., and Wilhelm, P.: Towards accurate and practical drone-based wind measurements with an ultrasonic anemometer, Atmospheric Measurement Techniques, 14, 1303–1318, https://doi.org/10.5194/amt-14-1303-2021, 2021.

van Hove, A., Aalstad, K., Lind, V., Arndt, C., Odongo, V., Ceriani, R., Fava, F., Hulth, J., and Pirk, N.: Inferring methane emissions from African livestock by fusing drone, tower, and satellite data, EGUsphere, 2025, 1–36, https://doi.org/10.5194/egusphere-2024-3994, 2025.

Vergassola, M., Villermaux, E., and Shraiman, B.: 'Infotaxis' as a strategy for searching without gradients., Nature, 445, 406–409, https://doi.org/https://doi.org/10.1038/nature05464, 2007.

Walter Anthony, K. M., Anthony, P., Grosse, G., and Chanton, J.: Geologic methane seeps along boundaries of Arctic permafrost thaw and melting glaciers, Nature Geoscience, 5, 419–426, https://doi.org/https://doi.org/10.1038/ngeo1480, 2012.

https://doi.org/10.5194/egusphere-2026-51
Preprint. Discussion started: 20 January 2026

Wesley, D., Dallimore, S., MacLeod, R., Sachs, T., and Risk, D.: Characterization of atmospheric methane release in the outer Mackenzie River delta from biogenic and thermogenic sources, The Cryosphere, 17, 5283–5297, https://doi.org/10.5194/tc-17-5283-2023, 2023.

Wetz, T., Wildmann, N., and Beyrich, F.: Distributed wind measurements with multiple quadrotor unmanned aerial vehicles in the atmospheric boundary layer, Atmospheric Measurement Techniques, 14, 3795–3814, https://doi.org/10.5194/amt-14-3795-2021, 2021.

Wetz, T., Zink, J., Bange, J., and Wildmann, N.: Analyses of Spatial Correlation and Coherence in ABL Flow with a Fleet of UAS, Boundary-Layer Meteorology, 187, 673–701, https://doi.org/10.1007/s10546-023-00791-4, 2023.

Wildmann, N. and Wetz, T.: Towards vertical wind and turbulent flux estimation with multicopter uncrewed aircraft systems, Atmospheric Measurement Techniques, 15, 5465–5477, https://doi.org/10.5194/amt-15-5465-2022, 2022.

Yazbeck, T., Schlutow, M., Bolek, A., Triches, N. Y., Wahl, E., Heimann, M., and Göckede, M.: Quantifying landcover-specific fluxes over a heterogeneous landscape through coupling UAV-measured mixing ratios with a large-eddy simulation model and Eddy-covariance measurements, Atmospheric Measurement Techniques, 18, 6917–6932, https://doi.org/10.5194/amt-18-6917-2025, 2025.

Zhang, M., Leifer, I., and Hu, C.: Challenges in methane column retrievals from AVIRIS-NG imagery over spectrally cluttered surfaces: A sensitivity analysis, Remote Sensing, 9, 835, 2017.